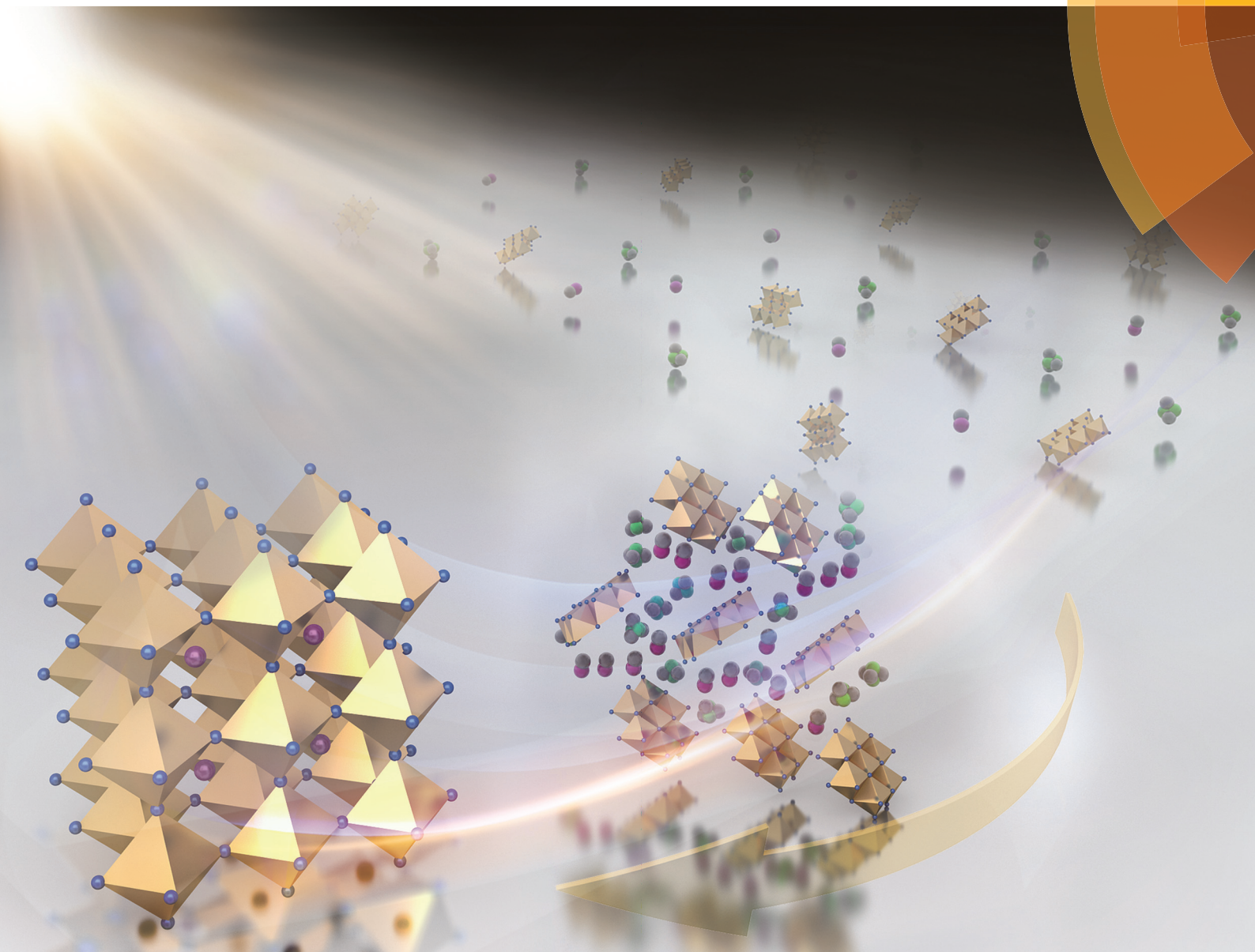


Nanoscale

www.rsc.org/nanoscale



ISSN 2040-3364



PAPER

Yan Yao *et al.*

Critical kinetic control of non-stoichiometric intermediate phase transformation for efficient perovskite solar cells





Cite this: *Nanoscale*, 2016, **8**, 12892

Critical kinetic control of non-stoichiometric intermediate phase transformation for efficient perovskite solar cells†

Yaoguang Rong,^{‡a} Swaminathan Venkatesan,^{‡a} Rui Guo,^b Yanan Wang,^a Jiming Bao,^a Wenzhi Li,^b Zhiyong Fan^c and Yan Yao^{*a,d}

Organometal trihalide perovskites (OTP) have attracted significant attention as a low-cost and high-efficiency solar cell material. Due to the strong coordination between lead iodide (PbI₂) and dimethyl sulfide (DMSO) solvent, a non-stoichiometric intermediate phase of MA₂Pb₃I₈(DMSO)₂ (MA = CH₃NH₃⁺) usually forms in the one-step deposition method that plays a critical role in attaining high power conversion efficiency. However, the kinetic understanding of how the non-stoichiometric intermediate phase transforms during thermal annealing is currently absent. In this work, we investigated such a phase transformation and provided a clear picture of three phase transition pathways as a function of annealing conditions. The interdiffusion of MAI and DMSO varies strongly with the annealing temperature and time, thus determining the final film composition and morphology. A surprising finding reveals that the best performing cells contain ~18% of the non-stoichiometric intermediate phase, instead of pure phase OTP. The presence of such an intermediate phase enables smooth surface morphology and enhances the charge carrier lifetime. Our results highlight the importance of the intermediate phase growth kinetics that could lead to large-scale production of efficient solution processed perovskite solar cells.

Received 19th January 2016,
Accepted 5th February 2016

DOI: 10.1039/c6nr00488a

www.rsc.org/nanoscale

Introduction

In the past three years, perovskite solar cells (PSCs) have attracted increasing attention due to their low material cost, simple fabrication process, and high power conversion efficiency (PCE).^{1–7} The organic–inorganic hybrid halide perovskites of methyl ammonium lead halides (MAPbX₃, MA = CH₃NH₃⁺, X = Cl[–], Br[–] or I[–]) possess exceptional properties for application in photovoltaics, such as a high extinction coefficient, long charge-carrier diffusion length, and low recombination rate along with a tunable bandgap.^{8–13} The optimization of perovskite film deposition approaches,^{3,14–17} design of new material systems,^{4,6–8} and diversity of device architectures^{18–22} have enabled the efficiency of PSCs to increase from 2.19% to

a certified 20.1%,⁴ making PSCs the fastest advancing photovoltaic technology to date.

Planar heterojunction (PHJ) PSCs simplify the device fabrication and enable low-temperature (<150 °C) solution processing.^{20,23,24} The surface quality of the perovskite layer in PHJ solar cells plays an important role in determining the device performance. A smooth, uniform and compact perovskite film is necessary to avoid the leakage current and absorption losses.^{8–10} Various deposition methods such as one-step deposition, two-step sequential deposition, vapour deposition *etc.* have been investigated to produce high-quality perovskite films.^{9,15–17} Among these methods, the formation of an intermediate phase to reduce the fast reaction between PbI₂ and MAI in common solvents has been found to be critical in obtaining smooth and compact perovskite films in one-step solution processing.^{6,14,25–29} However, there is no agreement regarding the crystal structure and chemical composition of the intermediate phase. Recently, the single crystal structure of the intermediate phase was obtained and the chemical formula was found to be non-stoichiometric as MA₂Pb₃I₈(DMSO)₂, in contrast to the previous reports of MAI–PbI₂–DMSO with 1 : 1 : 1 stoichiometry.^{6,14,27} However, the kinetic understanding of how the non-stoichiometric intermediate phase transforms during thermal annealing is currently missing.

^aDepartment of Electrical & Computer Engineering and Materials Science and Engineering Program, University of Houston, Houston, Texas 77204, USA.
E-mail: yyao4@uh.edu

^bDepartment of Physics, Florida International University, Miami, FL 33199, USA

^cDepartment of Electronic and Computer Engineering, Hong Kong University of Science and Technology, Clear Water Bay, Kowloon, Hong Kong SAR, China

^dTexas Center for Superconductivity at the University of Houston, Houston, Texas 77204, USA

†Electronic supplementary information (ESI) available. See DOI: 10.1039/c6nr00488a

‡These authors contributed equally to the work.

In this article, we investigate non-stoichiometric intermediate phase transitions during thermal annealing and provide a physical picture of three kinetics-determined reaction pathways as a function of annealing conditions. The kinetics of molecular exchange between dimethyl sulfoxide (DMSO) and MAX are supported by the structural and morphological changes and their correlation with the device performance. The presence of such an intermediate phase enables smooth surface morphology of the perovskite films and enhances the charge carrier lifetime of the devices. Surprisingly, the devices showing the highest efficiency contained $\sim 18\%$ of the non-stoichiometric intermediate phase, instead of the pure perovskite phase due to an optimum diffusion rate between DMSO in the intermediate phase and MAX.

Results and discussion

The planar heterojunction devices were fabricated with the configuration of ITO/PEDOT:PSS/CH₃NH₃PbI_{3-x}Cl_x/PCBM/BCP/Al (Fig. 1a). The perovskite (MAPbX₃) thin film was prepared *via* the solvent engineering process using an orthogonal solvent to quench the wet precursor films during the spin-coating process. During the high-speed (4000 rpm) spin-coating process, an orthogonal solvent (such as toluene,^{14,25} diethyl ether²⁷ or chlorinated solvents^{26,30}) was dripped on the spinning substrate to remove excess solvent that did not coordinate with PbI₂/MAI. In our case toluene was used as the orthogonal solvent and γ -butyrolactone (GBL): DMSO (7:3 v/v) was used as a co-solvent. This solvent quenching process led to the formation of a transparent homogeneous thin film of an intermediate phase. Upon annealing the intermediate phase films resulted in dark brown, smooth and reflective thin films.

In the cross-sectional SEM image of the device (Fig. 1b), the interfaces of PEDOT:PSS/perovskite/PCBM were clearly observed. Fig. 1c shows the J - V characteristics of the devices fabricated with different annealing temperatures (70–100 °C) for 5 minutes. The solar cell parameters are listed in Table 1. Without any annealing, the pure intermediate phase device demonstrated a poor photovoltaic response with a PCE of $\sim 0.05\%$ with a short-circuit current density (J_{sc}) of 0.12 mA cm⁻². The device efficiency increased to 9.29% after annealing at 70 °C for 5 min due to the conversion of the intermediate phase to the perovskite phase (*vide infra*). The optimal annealing temperature is found to be 90 °C, which shows a PCE of 15.29% with a V_{oc} of 1.00 V, a J_{sc} of 19.84 mA cm⁻² and a FF of 0.77. A set of devices were fabricated to study the effect of annealing temperature (70–100 °C) and annealing time (1–60 min). Fig. 1d shows the contour maps of PCE, V_{oc} , FF and J_{sc} with detailed photovoltaic parameters summarized in Table S1 (ESI†). Clearly, the highest efficiency of $\sim 15\%$ was achieved for samples annealed at 85–95 °C for 5–10 min. A small deviation from the optimum annealing conditions led to a substantial decrease in device performance.

Table 1 Photovoltaic parameters of devices fabricated with non-annealed and 70–100 °C (5 min) annealed films

| Device | V_{oc} [V] | J_{sc} [mA cm ⁻²] | FF | PCE [%] |
|--------------|--------------|---------------------------------|-------|---------|
| Non-annealed | 0.89 | 0.12 | 0.431 | 0.05 |
| 70 °C | 0.98 | 13.60 | 0.700 | 9.29 |
| 80 °C | 0.97 | 15.25 | 0.794 | 11.74 |
| 90 °C | 1.00 | 19.84 | 0.773 | 15.29 |
| 100 °C | 0.92 | 18.25 | 0.755 | 12.60 |

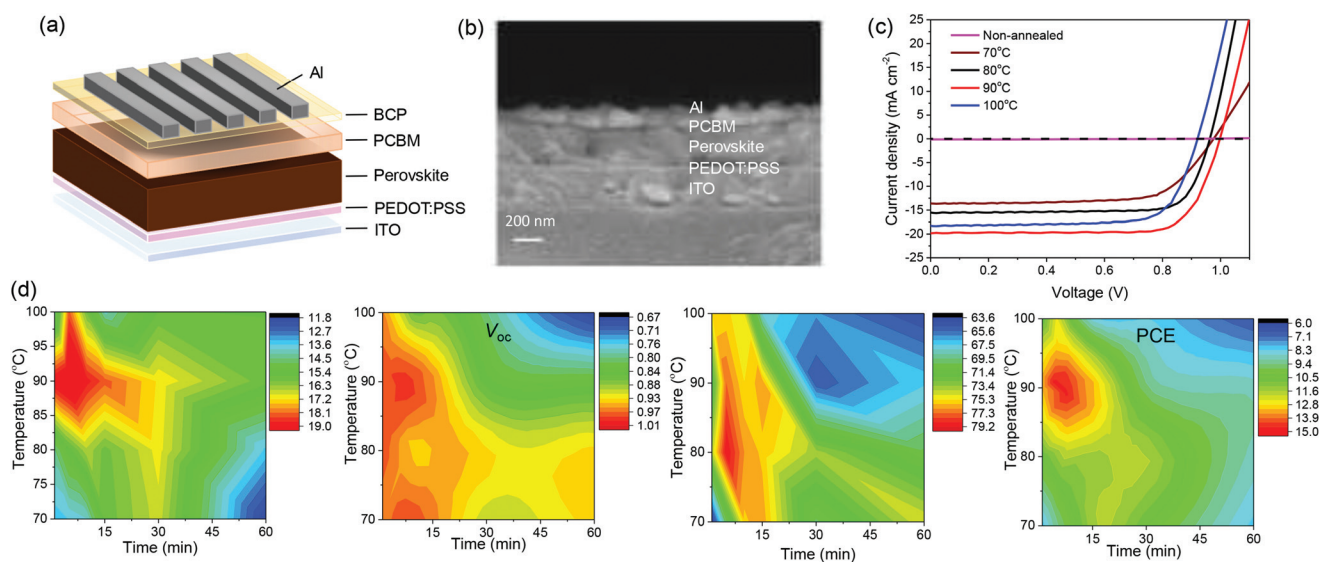


Fig. 1 (a) Device schematic of a PHJ solar cell with the configuration of ITO/PEDOT:PSS/perovskite/PCBM/BCP/Al. (b) Cross-sectional SEM image. (c) J - V curves of devices fabricated with annealed (70–100 °C for 5 min) and non-annealed films. (d) 2D contour of device photovoltaic parameters of J_{sc} , V_{oc} , FF and PCE with various annealing time and temperature.

To shed light on the role of thermal annealing on the phase composition, temperature dependent X-ray diffraction (XRD) was performed. All the films were prepared on PEDOT:PSS coated ITO substrates. The non-annealed samples showed identical peak positions compared to those observed in $\text{MA}_2\text{Pb}_3\text{I}_8(\text{DMSO})_2$ single crystals (Fig. 2a): the peaks at 6.76° , 7.46° and 9.38° correspond to the (002), (021) and (022) planes of $\text{MA}_2\text{Pb}_3\text{I}_8(\text{DMSO})_2$. Samples that were annealed between 70°C and 100°C demonstrated a transformation of the intermediate phase to the perovskite phase with a characteristic peak at 14.36° (Fig. 2b). Surprisingly, the intermediate phase (labelled as δ) was observed in the XRD patterns of all the annealed films. The ratio of such an intermediate phase was calculated by considering the (022) peak of $\text{MA}_2\text{Pb}_3\text{I}_8(\text{DMSO})_2$ to the (110) peak of perovskite MAPbX_3 , which was also confirmed by Energy Dispersive X-Ray (EDX) analysis, as shown in Fig. 2c and Table S2 (ESI[†]). As the annealing temperature increases, the intermediate phase fraction steadily decreases from $\sim 30\%$ at 70°C to $\sim 8\%$ at 100°C . Interestingly, $\sim 18\%$ of the intermediate phase still exists even for the thin films annealed at 90°C which shows 15% PCE. Further increasing the annealing time at 90°C and 100°C can reduce the ratio of the intermediate phase, along with the increase of PbI_2 (Fig. S1, ESI[†]). But at

70°C , the peak intensity of the intermediate phase showed almost no change even after 60 min, indicating that the intermediate phase in the perovskite thin film can be stable for potential applications. We also performed XRD after device testing to make sure no change in the phase composition takes place during electrode deposition, light soaking or current-voltage measurements (Fig. S2, ESI[†]). As shown in Fig. 2d, the non-annealed sample shows very low absorption between 450 nm and 800 nm, while the annealed sample shows stronger absorption with an onset at 750 nm.^{1,5,28,31} Similarly, the photoluminescence (PL) spectra (inset of Fig. 2d) display that annealed samples have a high PL intensity at 765 nm while non-annealed samples show no PL response. The absorption spectra of perovskite films annealed at different temperatures are presented in Fig. S3 (ESI[†]).

Fig. 3 shows the atomic force microscopy (AFM) and scanning electron microscopy (SEM) images of 80°C , 90°C and 100°C annealed films. A smooth surface having a root mean square (RMS) roughness of 10.2 nm and 12.3 nm is observed in the AFM images of 80°C and 90°C films respectively (Fig. 3a and b). When the annealing temperature was increased to 100°C , the surface morphology became rougher and several μm sized islands were formed. These islands had a

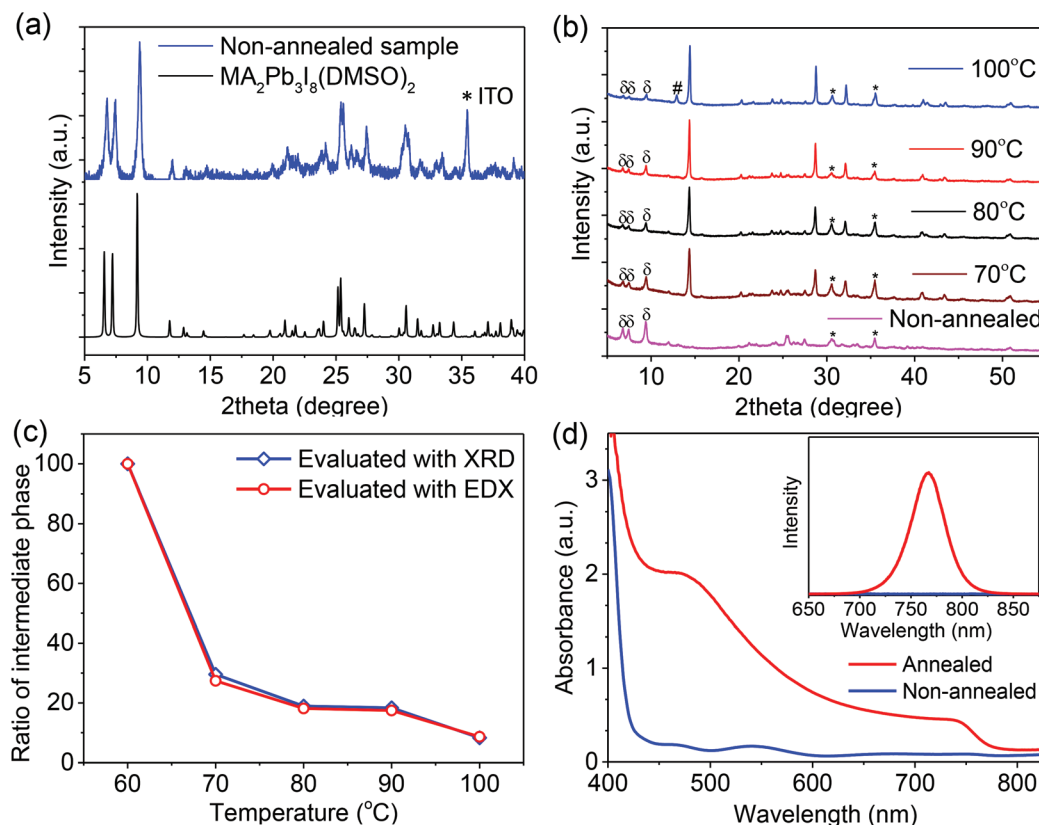


Fig. 2 (a) XRD spectra of an intermediate single crystal $\text{MA}_2\text{Pb}_3\text{I}_8(\text{DMSO})_2$ and a non-annealed sample deposited on the ITO substrate. (b) XRD spectra of $\text{MA}_2\text{Pb}_3\text{I}_8(\text{DMSO})_2$ intermediate phase films without annealing, annealed at 70°C , 80°C , 90°C and 100°C for 5 min; δ , # and * represent peaks for intermediate phase, PbI_2 and ITO, respectively. (c) Evolution of the ratio of the intermediate phase in the annealed films with annealing temperature. (d) UV-Visible spectra of the annealed and non-annealed intermediate phase films. Inset: steady-state photoluminescence (PL) spectra of the annealed and non-annealed intermediate phase films.

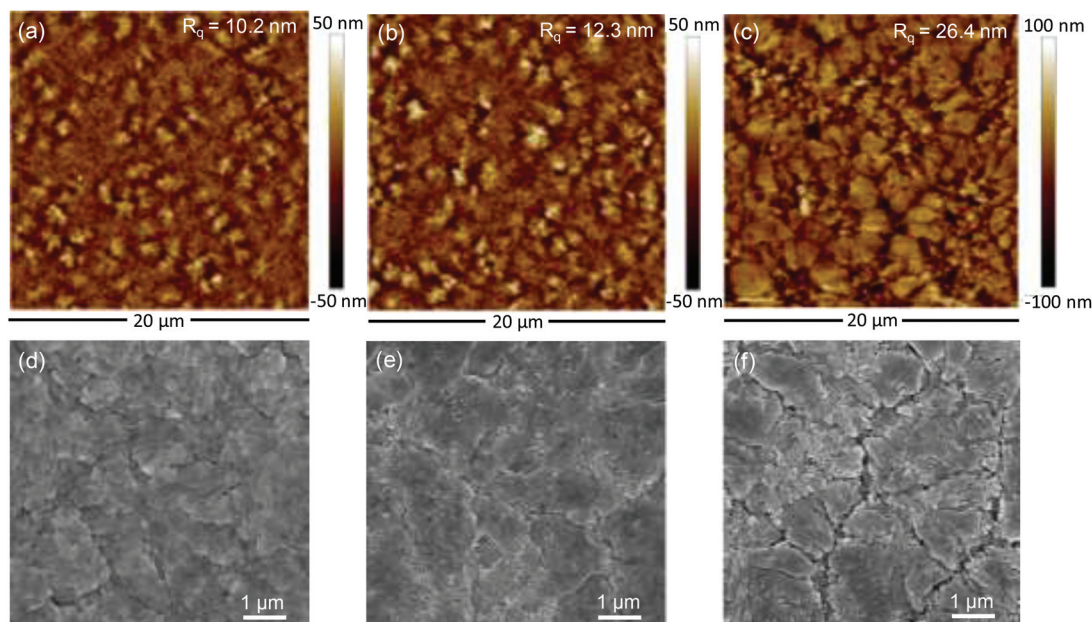


Fig. 3 AFM images of perovskite films annealed at 80 °C (a), 90 °C (b), and 100 °C (c); SEM images of perovskite films annealed at 80 °C (d), 90 °C (e), and 100 °C (f).

height of ~ 120 nm that led to an overall RMS roughness of 26.4 nm (Fig. 3c).

The SEM images also confirmed the same observation: a compact and smooth morphology for 80 °C and 90 °C annealed films (Fig. 3d and e) and deeper cracks for 100 °C annealed films (Fig. 3f). The high-magnification SEM image of the perovskite film annealed at 90 °C is shown in Fig. S4.† The film was quite homogeneous with the grain size between 200 and 400 nm, which is similar to the results in the literature.^{14,29} Increasing the annealing time (15 to 30 min) at 100 °C led to even rougher morphology (Fig. S5, ESI†), from which it can be understood that distinct PbI_2 peaks start to appear in 100 °C annealed films. Considering that the ultra-smooth films contained a small amount of the intermediate phase while the rough/cracked films contained excessive PbI_2 , and the poor photovoltaic performance and weak absorption of the intermediate phase, we believe that the phase does not contribute either to charge generation or transport and it merely functions as a morphology stabilizer.

It was observed that non-annealed films conform to the crystal structure and chemical composition of the MAI deficient $\text{MA}_2\text{Pb}_3\text{X}_8(\text{DMSO})_2$ phase and upon annealing resulted in the stoichiometric MAPbI_3 tetragonal perovskite phase. Therefore, it is expected that the uncoordinated MAI is either on the surface of the crystals or homogeneously distributed around the intermediate phase domains (Fig. 4a). Several reports that have studied the phase composition and reaction kinetics have shown that the perovskite phase should be stable at wider temperature ranges with less time dependency.^{17,20,32–34} However the sensitivity of conversion on the annealing time and temperature in our case leads us to the

hypothesis that the conversion mechanism is possibly due to intramolecular exchange^{4,35} between the DMSO molecules and uncoordinated MAI molecules and not due to the removal of DMSO as reported before.^{14,27} If only the removal of DMSO is responsible for the formation of the perovskite phase then only one factor between time and temperature would affect the phase conversion, *i.e.* either lower temperature and longer time or higher temperature and shorter time. It is likely that there are two processes involved which are time and temperature dependent. Annealing provides the thermal energy to drive the diffusion of each constituent and the diffusion kinetics determine the final phase composition of the film. This could also explain the higher annealing temperatures required for formamidinium lead iodide perovskite films deposited using the same solvent quenching method due to the larger size of the formamidinium iodide cation compared to methylammonium iodide.^{6,36} The possible diffusion pathways and kinetics are proposed in Fig. 4b. During the annealing process, the intermediate phase initially acts as a template or a framework for phase transformation. Lower annealing temperatures (<90 °C) lead to slow diffusion of DMSO molecules and incomplete conversion of the intermediate phase. Hence 70 °C and 80 °C annealed films showed a higher concentration of the intermediate phase and lower photocurrent in photovoltaic devices. When the annealing temperature and time were high (>90 °C and $t > 10$ min) faster diffusion of DMSO and sublimation of MAI/MACl lead to the formation of the PbI_2 phase.³⁷ Sublimation of MAI/MACl is supported by the XPS spectra that show two distinct Cl 2p peaks in films annealed at 90 °C and the peaks are suppressed in the 100 °C annealed films (Fig. S6, ESI†). Further, the formation of the PbI_2 phase results in

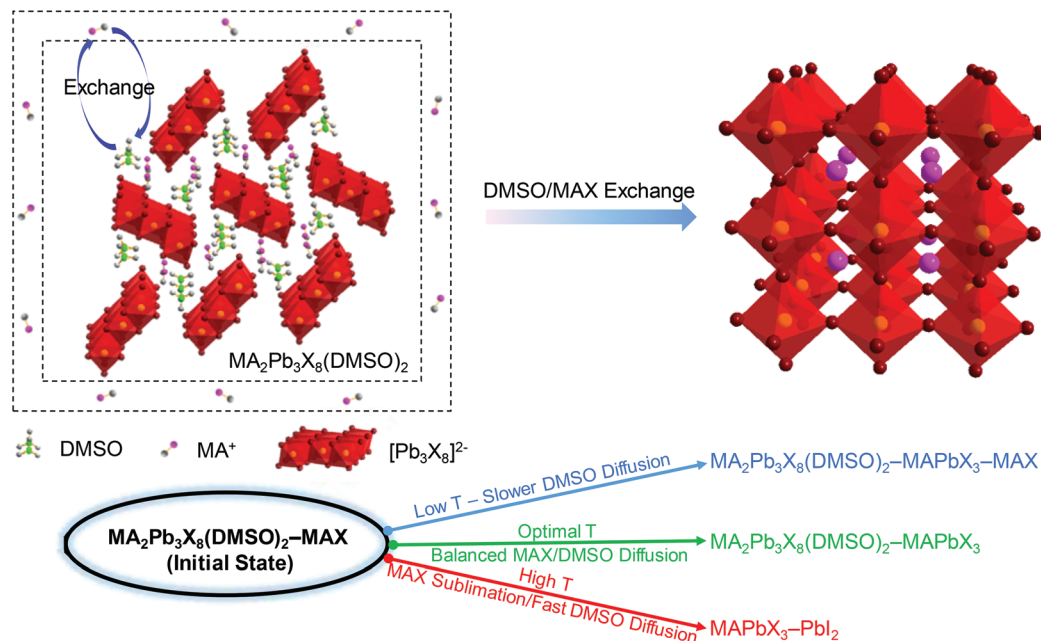


Fig. 4 (a) The schematic crystal structure and composition of the intermediate phase and perovskite phase. (b) Three diffusion pathways to final film composition depending on different annealing temperatures.

rougher morphology which eventually leads to lower FF and V_{oc} in solar cells. Under the optimized conditions, balanced diffusion of DMSO and MAI/MACI leads to enhanced conversion as well as smooth morphology ideal for planar hetero-junction solar cells. It is critical for the intermediate phase to co-exist in a small fraction with the final perovskite phase to avoid the formation of voids or gaps within the film.

Based on the previous discussions, 62 devices were fabricated using the optimal annealing conditions (90 °C for

5 min) to acquire perovskite active layer films with smooth morphology as well as optimal phase composition. Fig. 5a–d show the statistics of PCE, V_{oc} , J_{sc} and FF. The optimal annealing conditions led to an average PCE of 13.2%. The variation in efficiency is mainly determined by J_{sc} , presumably due to the change in composition arising from variations in delay time in the toluene washing step, which could possibly affect both the morphology and the phase composition.^{25–27} Fig. 5e shows the J - V curve of the champion cell with PCE of 15.29%,

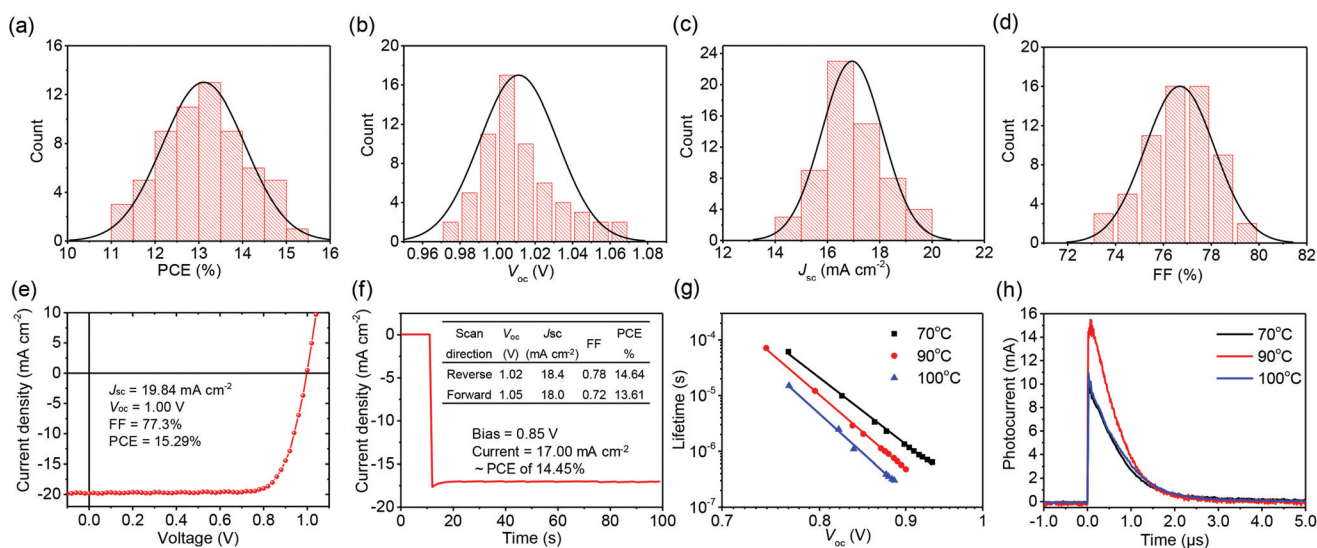


Fig. 5 Histograms of (a) PCE, (b) V_{oc} , (c) J_{sc} , (d) FF of the devices fabricated under optimal annealing conditions at 90 °C for 5 min. (e) Reverse J - V scan of the champion device. (f) Measured photocurrent vs. time at the maximum power point. (g) Transient photovoltage (TPV) measurement and (h) transient photocurrent (TPC) decay measurements for active layers annealed at 70 °C, 90 °C and 100 °C, respectively.

J_{sc} of 19.84 mA cm⁻², V_{oc} of 1.00 V and FF of 0.77. The corresponding shunt resistance and series resistance are 5.99 kΩ cm² and 4.20 Ω cm², which are comparable to the values reported for the best devices.^{17,38,39} Photocurrent hysteresis may exist in perovskite devices, which is strongly dependent on the device fabrication process, contact material, and device architecture as well as the scanning rate and directions in the measurement.⁴⁰⁻⁴² Only minimal hysteresis was observed in our samples where reverse scanning showed slightly larger FF while forward scanning showed slightly higher V_{oc} . We measured the photocurrent as a function of time at the maximum power point at ~0.85 V (Fig. 5f). The photocurrent density arises to ~17.00 mA cm⁻² within seconds, indicating a negligible amount of charge traps¹⁷ and then stabilizes for 100 seconds. The calculated efficiency of 14.45% confirms that the efficiency measured with reverse scan in the J - V test is closer to the accurate value (Fig. S7, ESI†).

In order to further examine the effect of morphology and phase composition on charge transport, the charge recombination and charge transport were measured by transient photovoltage (TPV) and transient photocurrent (TPC) decay (Fig. 5g-h). It is clearly observed that devices fabricated with perovskite layers annealed at 70 °C and 90 °C have a longer lifetime throughout the entire V_{oc} range compared to that annealed at 100 °C. Particularly, the charge-recombination lifetimes of the 70 °C, 90 °C and 100 °C annealed devices are 2.29 μs, 2.05 μs and 1.10 μs respectively under 0.22 sun illumination intensity, which are comparable to the literature results.^{17,38} The enhanced lifetime for lower temperatures annealed perovskite devices are mainly due to smoother morphology and less defective interfaces. It is noteworthy to point out that the 70 °C annealed device with a slightly longer lifetime is due to the low charge carrier concentration observed as the lower J_{sc} in Fig. 5h because it is known that the recombination rate is highly dependent on the charge carrier concentration.^{43,44} For the 100 °C annealed device, the shorter lifetime and lower V_{oc} are attributed to the enhanced recombination at the decomposed perovskite (PbI₂)/PCBM interface. In transient photocurrent measurements, the highest photocurrent peak with the shortest charge collection time of ~647 ns was observed for the 90 °C annealed device (Fig. 5h). In comparison, devices with 70 °C annealed films showed the lowest photocurrent response with a charge collection time of ~707 ns. The 100 °C annealed devices showed a slightly higher photocurrent peak while having a longer collection time of ~764 ns. A longer charge collection time is attributed to the higher series resistance observed in 70 °C and 100 °C annealed devices and the peak photocurrent trend is similar to the trend in J_{sc} for the tested devices.

Conclusions

We found that the phase composition and morphology of solvent engineered perovskite films are strongly dependent on the processing conditions and can significantly influence the

photovoltaic performance. The strong dependence on processing conditions is attributed to the molecular exchange kinetics between organic halide molecules and DMSO coordinated in the intermediate phase. Through XRD and morphology characterization we found that slower diffusion of DMSO leads to a higher fraction of the intermediate phase and smoother surface morphology. While photovoltaic devices with smoother morphology exhibit a higher charge carrier lifetime and fill factor, an excessive amount of the intermediate phase suppresses the charge carrier density. Optimal annealing conditions lead to balanced diffusion and a smooth morphology to realize the highest photovoltaic efficiency. These findings highlight the importance of phase and kinetics control in obtaining high efficiency inorganic-organic lead halide perovskite materials for photovoltaic applications.

Experimental

Materials and methods

Lead iodide (PbI₂), lead chloride (PbCl₂), γ -butyrolactone (GBL), dimethylsulfoxide (DMSO) and toluene were purchased from Sigma-Aldrich and used without further purification. Methylammonium iodide (MAI) was synthesized according to the literature.³ The precursor solution was prepared by dissolving MAI (1.30 M), PbI₂ (1.26 M) and PbCl₂ (0.14 M) in the DMSO/GBL mixed solvent (3 : 7 v/v) and stirring at 70 °C for 3 h.

Device fabrication

PEDOT:PSS layer was spun on cleaned ITO substrates at 4000 rpm for 30 s after UV-ozone treatment for 15 min, and dried at 120 °C for 20 min. The perovskite precursor solution was spun on top of the PEDOT:PSS layer at 1000 rpm for 10 s and 4000 rpm for 25 s. During the 4000 rpm spin-coating process, toluene (200 μl) was dripped onto the center of the spinning substrate with a delay time of 20 s. After toluene dripping, the intermediate phase films were transferred to the hot plate immediately and annealed at 70–100 °C for 1–60 min to form perovskite films. After cooling down to room temperature, chlorobenzene (CB) solution (20 mg ml⁻¹) of PC₆₁BM was spun on top of the perovskite films at 1000 rpm for 40 s and annealed at 80 °C for 20 min. Finally, 8 nm thick bathocuproine (BCP) and 100 nm thick Al were thermal evaporated with a mask under high vacuum (2×10^{-6} Pa). The active device area is 0.09 cm².

Measurement and characterization

The X-ray diffraction (XRD) spectra were recorded using a Rigaku diffractometer with Cu K α radiation (1.5405 Å). The ultraviolet-visible (UV-Vis) absorption spectra were recorded using an Agilent spectrophotometer (Cary 60). Atomic Force Microscopy (AFM) tests were performed using the Bruker Innova-IRIS AFM system in tapping mode. The current density-voltage (J - V) characteristics were measured using a Keithley 2400 source-meter under AM1.5G illumination at

100 mW cm⁻² from a Newport solar simulator calibrated with a Si diode (KG-5 filter). The *J*-*V* curves were obtained through reverse scan (1.2 V to -0.2 V) and forward scan (-0.2 V to 1.2 V) with a step size of 20 mV and the delay time of 50 ms. Transient photovoltage (TPV) and transient photocurrent (TPC) decay was carried out using a NL 100 nitrogen laser incident on the device. The background intensity was varied using a Thorlabs filter wheel. Voltage decay was recorded on a Keysight (Agilent) MSOX4154A oscilloscope. The waveforms were averaged for 20 pulses and fitted with mono-exponential decay to calculate the charge carrier lifetime.

Acknowledgements

Y.Y. acknowledges the TcSUH award for the financial support. We thank Benjamin Emley for proofreading the manuscript.

Notes and references

- H.-S. Kim, C.-R. Lee, J.-H. Im, K.-B. Lee, T. Moehl, A. Marchioro, S.-J. Moon, R. Humphry-Baker, J.-H. Yum, J. E. Moser, M. Grätzel and N.-G. Park, *Sci. Rep.*, 2012, **2**, 591.
- M. M. Lee, J. Teuscher, T. Miyasaka, T. N. Murakami and H. J. Snaith, *Science*, 2012, **338**, 643–647.
- J. Burschka, N. Pellet, S.-J. Moon, R. Humphry-Baker, P. Gao, M. K. Nazeeruddin and M. Grätzel, *Nature*, 2013, **499**, 316–319.
- W. S. Yang, J. H. Noh, N. J. Jeon, Y. C. Kim, S. Ryu, J. Seo and S. I. Seok, *Science*, 2015, **348**, 1234–1237.
- M. A. Green, A. Ho-Baillie and H. J. Snaith, *Nat. Photonics*, 2014, **8**, 506–514.
- N. J. Jeon, J. H. Noh, W. S. Yang, Y. C. Kim, S. Ryu, J. Seo and S. I. Seok, *Nature*, 2015, **517**, 476–480.
- Y. Rong, Z. Ku, A. Mei, T. Liu, M. Xu, S. Ko, X. Li and H. Han, *J. Phys. Chem. Lett.*, 2014, **5**, 2160–2164.
- J. H. Noh, S. H. Im, J. H. Heo, T. N. Mandal and S. I. Seok, *Nano Lett.*, 2013, **13**, 1764–1769.
- G. E. Eperon, S. D. Stranks, C. Menelaou, M. B. Johnston, L. M. Herz and H. J. Snaith, *Energy Environ. Sci.*, 2014, **7**, 982–988.
- G. Xing, N. Mathews, S. S. Lim, N. Yantara, X. Liu, D. Sabba, M. Grätzel, S. Mhaisalkar and T. C. Sum, *Nat. Mater.*, 2014, **13**, 476–480.
- J.-H. Im, C.-R. Lee, J.-W. Lee, S.-W. Park and N.-G. Park, *Nanoscale*, 2011, **3**, 4088–4093.
- Q. Dong, Y. Fang, Y. Shao, P. Mulligan, J. Qiu, L. Cao and J. Huang, *Science*, 2015, **347**, 967–970.
- G. Xing, N. Mathews, S. Sun, S. S. Lim, Y. M. Lam, M. Grätzel, S. Mhaisalkar and T. C. Sum, *Science*, 2013, **342**, 344–347.
- N. J. Jeon, J. H. Noh, Y. C. Kim, W. S. Yang, S. Ryu and S. I. Seok, *Nat. Mater.*, 2014, **13**, 897–903.
- Q. Chen, H. Zhou, Z. Hong, S. Luo, H.-S. Duan, H.-H. Wang, Y. Liu, G. Li and Y. Yang, *J. Am. Chem. Soc.*, 2013, **136**, 622–625.
- M. Liu, M. B. Johnston and H. J. Snaith, *Nature*, 2013, **501**, 395–398.
- Z. G. Xiao, C. Bi, Y. C. Shao, Q. F. Dong, Q. Wang, Y. B. Yuan, C. G. Wang, Y. L. Gao and J. S. Huang, *Energy Environ. Sci.*, 2014, **7**, 2619–2623.
- J. Y. Jeng, Y. F. Chiang, M. H. Lee, S. R. Peng, T. F. Guo, P. Chen and T. C. Wen, *Adv. Mater.*, 2013, **25**, 3727–3732.
- A. Mei, X. Li, L. Liu, Z. Ku, T. Liu, Y. Rong, M. Xu, M. Hu, J. Chen, Y. Yang and H. Han, *Science*, 2014, **345**, 295–298.
- H. Zhou, Q. Chen, G. Li, S. Luo, T.-b. Song, H.-S. Duan, Z. Hong, J. You, Y. Liu and Y. Yang, *Science*, 2014, **345**, 542–546.
- K. Wang, C. Liu, P. Du, J. Zheng and X. Gong, *Energy Environ. Sci.*, 2015, **8**, 1245–1255.
- M. M. Tavakoli, K.-H. Tsui, Q. Zhang, J. He, Y. Yao, D. Li and Z. Fan, *ACS Nano*, 2015, **9**, 10287–10295.
- J. You, Z. Hong, Y. Yang, Q. Chen, M. Cai, T.-B. Song, C.-C. Chen, S. Lu, Y. Liu and H. Zhou, *ACS Nano*, 2014, **8**, 1674.
- P. Docampo, J. M. Ball, M. Darwich, G. E. Eperon and H. J. Snaith, *Nat. Commun.*, 2013, **4**, 2761.
- Y. Rong, Z. Tang, Y. Zhao, X. Zhong, S. Venkatesan, H. Graham, M. Patton, Y. Jing, A. M. Guloy and Y. Yao, *Nanoscale*, 2015, **7**, 10595–10599.
- M. D. Xiao, F. Z. Huang, W. C. Huang, Y. Dkhissi, Y. Zhu, J. Etheridge, A. Gray-Weale, U. Bach, Y. B. Cheng and L. Spiccia, *Angew. Chem., Int. Ed.*, 2014, **53**, 9898–9903.
- N. Ahn, D. Y. Son, I. H. Jang, S. M. Kang, M. Choi and N. G. Park, *J. Am. Chem. Soc.*, 2015, **137**, 8696–8699.
- K. Sun, J. Chang, F. H. Isikgor, P. Li and J. Ouyang, *Nanoscale*, 2015, **7**, 896–900.
- J. Seo, S. Park, Y. C. Kim, N. J. Jeon, J. H. Noh, S. C. Yoon and S. I. Seok, *Energy Environ. Sci.*, 2014, **7**, 2642–2646.
- J. W. Jung, S. T. Williams and A. K. Y. Jen, *RSC Adv.*, 2014, **4**, 62971–62977.
- F. Hao, C. C. Stoumpos, Z. Liu, R. P. H. Chang and M. G. Kanatzidis, *J. Am. Chem. Soc.*, 2014, **136**, 16411–16419.
- C. Bi, Y. Shao, Y. Yuan, Z. Xiao, C. Wang, Y. Gao and J. Huang, *J. Mater. Chem. A*, 2014, **2**, 18508–18514.
- G. E. Eperon, V. M. Burlakov, P. Docampo, A. Goriely and H. J. Snaith, *Adv. Funct. Mater.*, 2014, **24**, 151–157.
- H. Yu, F. Wang, F. Xie, W. Li, J. Chen and N. Zhao, *Adv. Funct. Mater.*, 2014, **24**, 7102–7108.
- W. Li, J. Fan, J. Li, Y. Mai and L. Wang, *J. Am. Chem. Soc.*, 2015, **137**, 10399–10405.
- J. Seo, N. J. Jeon, W. S. Yang, H.-W. Shin, T. K. Ahn, J. Lee, J. H. Noh and S. I. Seok, *Adv. Energy Mater.*, 2015, **5**, 1501320.
- S. T. Williams, F. Zuo, C.-C. Chueh, C.-Y. Liao, P.-W. Liang and A. K. Y. Jen, *ACS Nano*, 2014, **8**, 10640–10654.
- Z. Xiao, Q. Dong, C. Bi, Y. Shao, Y. Yuan and J. Huang, *Adv. Mater.*, 2014, **26**, 6503–6509.

- 39 C. Bi, Q. Wang, Y. Shao, Y. Yuan, Z. Xiao and J. Huang, *Nat. Commun.*, 2015, **6**, 7747.
- 40 H. J. Snaith, A. Abate, J. M. Ball, G. E. Eperon, T. Leijtens, N. K. Noel, S. D. Stranks, J. T.-W. Wang, K. Wojciechowski and W. Zhang, *J. Phys. Chem. Lett.*, 2014, **5**, 1511–1515.
- 41 E. L. Unger, E. T. Hoke, C. D. Bailie, W. H. Nguyen, A. R. Bowring, T. Heumüller, M. G. Christoforo and M. D. McGehee, *Energy Environ. Sci.*, 2014, **7**, 3690–3698.
- 42 R. S. Sanchez, V. Gonzalez-Pedro, J.-W. Lee, N.-G. Park, Y. S. Kang, I. Mora-Sero and J. Bisquert, *J. Phys. Chem. Lett.*, 2014, **5**, 2357–2363.
- 43 Y. Zhao, A. M. Nardes and K. Zhu, *J. Phys. Chem. Lett.*, 2014, **5**, 490–494.
- 44 D. Bi, L. Yang, G. Boschloo, A. Hagfeldt and E. M. Johansson, *J. Phys. Chem. Lett.*, 2013, **4**, 1532–1536.